

Tailoring the Electronic Structure of Ir Alloy Electrocatalysts through Lanthanide (La, Ce, Pr, and Nd) for Acidic Oxygen Evolution Enhancement

Shuai Zhang, Mingzi Sun, Leilei Yin, Siyuan Wang, Bolong Huang,* Yaping Du,* and Chun-Hua Yan

The oxygen evolution reaction (OER) is critical for renewable energy conversion and storage devices. However, the rational design of electrocatalysts with suitably high efficiency and stability in strongly acidic electrolytes remains a major challenge. Herein, a solid-phase synthesis strategy is developed for the preparation of Ir-Ln (Ln = La, Ce, Pr, Nd) alloy nanoparticles with uniform particle size on carbon supports as superior acidic OER catalysts. Tailoring by the rare earth (RE) elements, Ir₂Pr achieves a maximum mass activity of 2.10 A mg⁻¹_{Ir} at 300 mV overpotential and stability over 200 h at 10 mA cm⁻² in 0.5 M H₂SO₄, which is 9.5 and 20 times higher to pure Ir nanoparticles. Furthermore, Ir₂Pr alloy nanoparticles exhibit excellent durability in strongly acidic electrolytes. Theoretical calculations have confirmed that the OER performances are strongly related to the RE elements in the alloy, where the d-band centers show a consistent trend with the overpotential. Moreover, the highest electroactivity of Ir₂Pr is attributed to the improved electron transfer by 4f orbitals and the suitable binding strength of intermediates. Herein, a fundamental understanding of the lanthanide–electrochemical performance relationship is provided and will also inspire the rational design of efficient nanoscale RE alloy electrocatalysts.

membrane (PEM) water electrolysis in acidic electrolytes can achieve much higher current densities than conventional alkaline electrolytes due to lower resistive losses and lower gas transitions.^[3–5] However, the oxygen evolution reaction (OER), which is the key and bottleneck reaction, has a high catalytic overpotential due to the slow four-electron transfer process with multiple oxygen intermediates, which severely hinders the overall efficiency.^[6,7] In addition, the poor stability of many OER catalysts in acidic solutions poses further challenges to the design of advanced catalysts, in which Ir-based materials are the only known practical industrial OER electrocatalysts.^[8,9] However, the low abundance amount of Ir and the current Ir-based catalysts still suffer from low mass activity, which cannot meet the requirements for high-performance and long-term stability at commercial current densities.^[10,11] For these reasons, the development of robust and activity-tunable

Ir-based catalysts is required to enhance OER performance.^[12]

Theoretical and experimental studies have shown that alloying provides a route to tune the electronic structure of noble metals to enhance catalytic performance.^[13] Alloying Ir with 3d transition metals such as Fe, Co, Ni, and Cu could induce electron redistribution of the Ir-5d orbital, resulting in its orbital being

1. Introduction

The production of fuels and chemicals from renewable solar and wind energy through emerging electrochemical technologies offers a promising solution to the energy crisis and environmental challenges.^[1,2] Hydrogen production using proton exchange

S. Zhang, L. Yin, S. Wang, Y. Du, C.-H. Yan
Tianjin Key Lab for Rare Earth Materials and Applications
Center for Rare Earth and Inorganic Functional Materials
School of Materials Science and Engineering
National Institute for Advanced Materials
Nankai University
Tianjin 300350, China
E-mail: ypdu@nankai.edu.cn

 The ORCID identification number(s) for the author(s) of this article can be found under <https://doi.org/10.1002/aesr.202300023>.

© 2023 The Authors. Advanced Energy and Sustainability Research published by Wiley-VCH GmbH. This is an open access article under the terms of the Creative Commons Attribution License, which permits use, distribution and reproduction in any medium, provided the original work is properly cited.

DOI: 10.1002/aesr.202300023

M. Sun, B. Huang
Department of Applied Biology and Chemical Technology
The Hong Kong Polytechnic University
Hung Hom, Kowloon 999077, Hong Kong SAR, China
E-mail: bhuang@polyu.edu.hk

B. Huang
Research Centre for Carbon-Strategic Catalysis
The Hong Kong Polytechnic University
Hung Hom, Kowloon 999077, Hong Kong SAR, China

C.-H. Yan
College of Chemistry and Chemical Engineering
Lanzhou University
Lanzhou 730000, China

partially occupied and the displacement of the d-band center, optimizing its bonding strength for adsorption.^[10,14] Despite the enhanced intrinsic activity of each active site in the catalyst, these alloys can suffer from severe dealloying problems, especially in harsh acidic solutions, resulting in diminished long-term stability. In recent years, rare earth (RE) alloys have attracted research interest due to their unusually negative alloy formation energies that are inherently less dealloying and exhibit high stability in acidic media.^[15–18] In addition to the excellent stability, RE elements have lanthanide contraction, and the lanthanide radius decreases with increasing f-shell filling, which allows RE elements to precisely tailor the electronic structure of active metals within a certain range. For example, in the oxygen reduction reaction, lanthanide contraction in Pt-lanthanide alloys controls the lattice spacing of the alloys and tunes the activity, stability, and reactivity of Pt.^[15] From an economic point of view, alloying Ir with RE elements can also reduce the use of Ir. For example, the current prices of metals La and Nd are less than 0.001% and 0.14% of Ir metal.^[17] However, limited by efficient synthetic methods, only the electrochemical activity of Pt-RE alloys has been investigated in the past decade, and the properties of Ir-RE nanoalloys have largely remained unexplored.^[19] Since RE elements are oxophilic, Ir, and RE elements have drastically different standard reduction potentials (e.g., +1.15 V for Ir³⁺/Ir and –2.38 V for La³⁺/La), which makes synthetic strategies in aqueous or protic solvents difficult to synthesize RE alloys. Therefore, it is highly desirable to develop an effective synthetic strategy for Ir-Ln alloys to achieve efficient and robust OER catalysts while revealing the interaction mechanism between RE and Ir.

Herein, a solid-phase synthesis strategy is developed for the preparation of uniform particle-size Ir-Ln alloys on graphene as superior acidic OER catalysts. Graphene, H₂IrCl₆·6H₂O, LnCl₃, and cyanamide were uniformly mixed as precursors by grinding, and sodium vapor was used as a reducing agent due to its strong reducing effect. After annealing, washing, and drying, a series of Ir-Ln/G (Ir₂La/G, Ir₂Ce/G, Ir₂Pr/G, and Ir₂Nd/G) nano-alloy catalysts can be obtained. The catalytic performance of Ir is enhanced by alloying with lanthanides. Benefiting from the lanthanide contraction of La≈Nd, the precise customization of the electronic structure of Ir is realized. Most importantly, the overpotential of Ir₂Pr is only 260 mV at 0.5 M H₂SO₄, which exceeds that of Ir/C and other Ir alloy nanocatalysts with different molar ratios. Meanwhile, a representative Ir₂Pr/G catalyst exhibits a high-quality activity of 2.10 A mg^{–1} noble metal at 1.53 V, which is 9.5 times that of Ir/G, while the stability reaches 200 h. Benefiting from the well-defined stoichiometric ratio and atomically ordered alloy structure, Ir₂Ln becomes a reliable model catalyst. Density functional theory (DFT) calculations have demonstrated that the Ir₂Ln alloys display volcano plots of the OER performances, which are determined by the valley trends of the d-band center. The introduced 4f orbitals in Ir₂Pr can alleviate the barrier of electron transfer from the electroactive Ir sites to the intermediates, leading to the smallest overpotential of OER.

2. Results and Discussion

The synthesis of nanoscale RE alloys is promising for practical industrial applications, but its synthesis is indeed challenging.

Due to the low reduction potential of RE ions, as shown in Figure S1a, Supporting Information, it is difficult to be simultaneously reduced and alloyed with transition metal ions, which makes the kinetic energy barrier in the synthesis process of RE alloys and late transition metal alloys different. Late transition metal alloys can be synthesized by conventional wet chemical techniques in aqueous or protic solvents, resulting in disordered solid solution alloys under mild conditions. The higher diffusion barrier needs to be overcome only when the synthesis of atomically ordered intermetallic compounds is required (Figure S1b, Supporting Information).^[20] Different from late transition metal alloys, RE elements need to overcome higher energy barriers even to form disordered alloys. This energy barrier is mainly composed of two parts, one part comes from the barrier that RE ions are reduced to metal states, and the other part is attributed to the mutual diffusion barrier of atoms in two metal states. In addition, the electronegativity difference between RE elements and late transition metals is large (e.g., 1.10 for La, 1.9 for Cu, 2.2 for Ir, and 2.2 for Pt), which leads to abnormally negative alloying energies.^[21] Therefore, after overcoming the energy barrier of alloying, the RE alloys are thermodynamically more inclined to form intermetallic compounds as shown in Figure S1c, Supporting Information. To overcome the barriers to RE alloying, a solid-phase synthesis strategy was developed for the preparation of Ir-Ln alloys with uniform particle size on graphene (Figure 1a). A homogeneous mixture of graphene, H₂IrCl₆·6H₂O, LnCl₃, and cyanamide was used as the precursor, and sodium vapor was employed as the reducing agent due to its strong reducing effect. After annealing, pickling, and drying, a series of Ir-Ln/G nano-alloy catalysts could be obtained.

The products were analyzed by powder X-Ray diffraction (XRD), inductively coupled plasma atomic emission spectroscopy (ICP-AES), high-resolution transmission electron microscopy (HR-TEM), and elemental mapping. Figure S2, Supporting Information shows the XRD patterns of the four alloy samples. The diffraction peaks of the samples are assigned to (1 1 1), (2 2 0), (3 1 1), (2 2 2), (4 0 0), (3 3 1), (5 1 1), (4 4 0), (5 3 3), and (6 2 2) crystal planes. They match well with the Inorganic Crystal Structure Database (ICSD) card for the ordered intermetallic phase, and the four Ir₂Ln/G alloys have similar unit cell structures, all of the Cubic Fd-3m space group.^[22–24] In addition, quantitative ICP-AES analysis was performed on the chemical composition of the nanoalloys (see Table S1, Supporting Information for the results of ICP-AES), and the results confirmed the molar ratio of Ir to RE elements in the samples was very close to 2:1. Figure 1b,c shows typical scanning transmission electron microscopy (STEM) and TEM images of the as-prepared Ir₂Pr/G. The Ir₂Pr alloy consists of small particles of a few nanometers in size with an average diameter of 7.3 nm and narrow size distribution (Figure S3, Supporting Information). As shown in Figure 1d, HR-TEM revealed that the lattice distance of the alloy particles was 0.27 nm and 0.44 nm, and the angle between the intersectant lattice fringes was 90°, corresponding to the (220) and (11) plane of the cubic phase Ir₂.^[24] All Ir₂Pr nanoparticles showed clear lattice fringes, indicating good crystallinity. The atomic model of Ir₂Pr further confirms the existence of the (11) plane, indicating the ordered structure of the Ir₂Pr alloy. Meanwhile, the corresponding element map images of Ir₂Pr/G confirmed the uniform

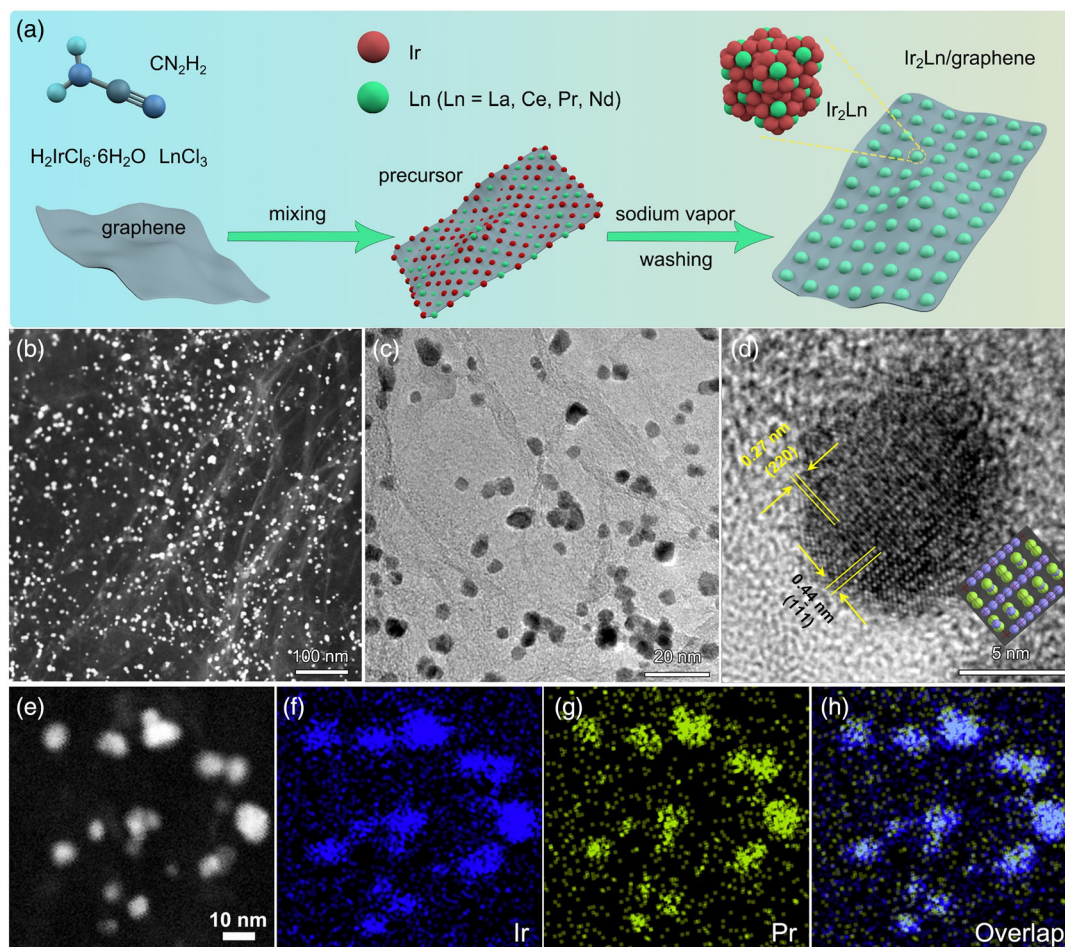


Figure 1. a) Schematic illustration of the synthesis method for Ir-Ln alloys (Ln = La, Ce, Pr, Nd) on graphene; b) HAADF-STEM image of Ir₂Pr/G sample; c) TEM image of Ir₂Pr/G sample; d) high-resolution TEM image of Ir₂Pr/G sample, inset is the atomic model of Ir₂Pr, green and blue spheres represent Pr and Ir atoms, respectively; e–g) the corresponding EDX elemental mappings of Ir₂Pr/G sample.

distribution of Ir and Pr elements (Figure 1e–f). In addition, TEM analysis of the remaining alloys was performed. All synthesized alloys had uniform shapes and sizes (Figure S4, Supporting Information). HR-TEM images of Ir₂La/G, Ir₂Pr/G, and Ir₂Nd/G samples all show a lattice spacing of 0.23 nm, corresponding to their (311) planes. In particular, the additionally exposed crystal plane is also consistent with the crystal structure.

To determine the surface electronic structure and chemical state of the fabricated alloy samples and the synthesized Ir/G nanocatalysts, X-Ray photoelectron spectroscopy (XPS) analysis was performed, and Ir 4*f* and La 3*d*, Ce 3*d*, Pr 3*d* XPS spectra were collected (Figure 2). Figure 2a shows the Ir 4*f* XPS spectrum, the two sets of double peaks at 61.3 and 64.3 eV, 62.7 and 65.7 eV, respectively, can be assigned to the Ir⁰ and Ir⁴⁺ valence states, indicating that there is partial spontaneous oxidation of Ir on the alloy surface.^[25] Compared with the Ir 4*f* signal of Ir/G that indicates the Ir⁴⁺ valence state, the Ir 4*f* signal of the Ir alloy shifts to lower binding energy, which indicates the electron transfer from La, Ce, Pr, and Nd to Ir in the alloy. More importantly, as the atomic number of Ln increases, the binding energy of Ir exhibits a regular red negative shift, which decreases

by −0.3 eV for Ir₂Nd/G and −0.1 eV for Ir₂La/G, indicating that lanthanide contraction provides an effective route for Ir electronic structure design (11). In the Pr 3*d* spectrum of Ir₂Pr/G, there are spin doublets at 954.7 eV (Pr 3*d*_{3/2}) and 934.6 eV (Pr 3*d*_{5/2}), and the Δ*E* of the main peak is 20.8 eV, indicating that the Pr is mainly in the metal valence state.^[26,27] The two weak peaks at 950.7 eV (Pr 3*d*_{3/2}) and 929.9 eV (Pr 3*d*_{5/2}) may be caused by the transfer of electrons from Pr to Ir through metallic bonds. As shown in Figure S5, Supporting Information, the Δ*E* values of La 3*d*, Ce 3*d*, and Nd 3*d* are 16.4, 18.3, and 22.4 eV, respectively, which are consistent with metallic La, Ce, and Nd, indicating that the Ln in the alloy is mainly zero valence state.^[28,29] The above results demonstrate the electronic effect of Ir-Ln alloys, electrons from La, Ce, Pr, or Nd are transferred to Ir, and alloying with lanthanides could effectively tailor the electronic structure of Ir.

To further analyze the electronic and local structure in the Ir₂Pr/G alloy, X-Ray absorption spectra were measured. Figure 2b shows the normalized Ir L₃ edge of the X-Ray near-edge structure absorption (XANES) spectra for Ir foil, Ir₂Pr/G, and IrO₂, located around 11215 eV, respectively. The intensity of the white line at the L₃ edge is closely related to the density

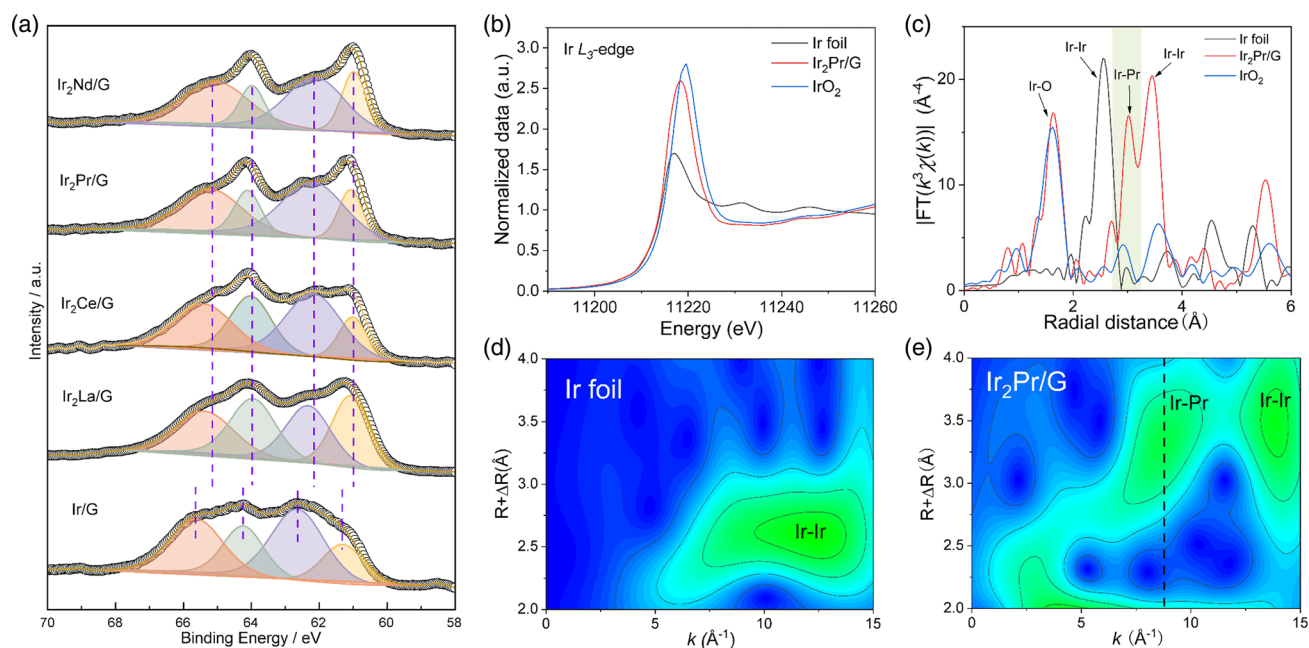


Figure 2. High-resolution XPS spectra and local structure analysis. a) Ir 4f of Ir₂La/G, Ir₂Ce/G, Ir₂Pr/G, Ir₂Nd/G samples, and Ir/G, b) Normalized Ir L₃edge XANES profiles of Ir₂Pr/G. The profiles of commercial Ir foil and IrO₂ are included as references, c) k³-Weighted Fourier transforms of EXAFS profiles of Ir₂Pr/G. The Ir foil data are multiplied by a factor of 0.4 for data display. The profiles of commercial Ir foil and IrO₂ are included as references. d,e) Wavelet-transformed EXAFS of Ir foil and Ir₂Pr/G, respectively.

of states of the d-band, which is an effective indicator of the valence state of 5d electronic materials.^[1] The Ir atom in IrO₂ exhibits the highest valence state and also the highest white line intensity. The white line intensity of Ir₂Pr/G is weaker than that of IrO₂, indicating that the average valence state of Ir in Ir₂Pr/G is lower than +4 valence, which is in good agreement with the XPS analysis. In addition, the white line intensity of Ir₂Pr/G is stronger than that of Ir foil, indicating that the alloying of Pr with Ir effectively tunes the d electron configuration of Ir, which helps to optimize the adsorption capacity of active O species during OER. The absorption edge energy of the corresponding sample was extracted using the first derivative of the spectrum. The k³-weighted Fourier transform of the extended X-Ray absorption fine structure (EXAFS) of the corresponding sample is shown in Figure 2c. The k-space EXAFS data are shown in Figure S6, Supporting Information and Table S2, Supporting Information. The presence of the Ir-O peak in the EXAFS curve of Ir₂Pr/G confirms the partial oxidation of Ir on the alloy surface. The peak at about 2.71 Å is assigned to the Ir-Ir shell, while the peak at about 1.62 Å is assigned to the Ir-O shell. For Ir₂Pr/G, two additional peaks appear around 3.0 and 3.4 Å, which can be assigned to the Ir-Pr shell and the Ir shell in the Ir₂Pr alloy. The peak around 1.9 Å can be assigned to the partial oxidation of Ir on the alloy surface. Furthermore, a wavelet transform was performed to visually examine the local coordination of Ir (Figure 2d,e), the maximum at 12.2 Å⁻¹ corresponds to the Ir-Ir coordination shell in the Ir foil, while the values at 9.0 and 13.9 Å⁻¹ correspond to the Ir-Pr coordination shell and Ir-Ir coordination shell in Ir₂Pr, respectively. These results

suggest that the alloying of Pr with Ir modulates the local coordination environment and electronic structure of Ir.

A typical three-electrode system was used in 0.5 M H₂SO₄ to study the effect of lanthanides in RE alloys on the OER properties of Ir, and the synthesized Ir/G was used as a reference. **Figure 3a** shows the linear sweep voltammetry (LSV) curves of various catalysts at 5 mV s⁻¹. It can be observed that the overpotentials at Ir-Ln/G current density of 10 mA cm⁻² are 318 mV (Ir₂La/G), 298 mV (Ir₂Ce/G), 260 mV (Ir₂Pr/G) and 274 mV (Ir₂Nd/G), much lower than Ir/G (371 mV), indicating that the presence of alloying Ln and Ir effectively enhances the OER activity in acidic media. Furthermore, as shown in Figure 3b, Ir-Ln/G exhibited lower Tafel slopes of 68.9~82.1 mV dec⁻¹ in the as-prepared electrocatalysts, suggesting that shrinking the lanthanide effectively tunes the reaction kinetics of Ir acidic OER learn. The double-layer capacitance (C_{dl}) of the catalyst is derived from the cyclic voltammetry (CV) curve (Figure 3c, Figure S7, Supporting Information). The electrochemical active surface area (ECSA) was calculated by dividing the integrated CO oxidation charge by 0.42 Mc cm⁻² (Figure S8, Supporting Information). The ECSA of Ir/G, Ir₂La/G, Ir₂Ce/G, Ir₂Pr/G, Ir₂Nd/G was 17.4, 59.7, 39.2, 95.2, 52.3 m² g⁻¹, respectively. By alloying with Ln, Ir₂Ln exposed more active sites. The change in Ir activity comes from the change in the electronic structure of Ln in the alloy, and the OER activity of Ir in the alloy is dependent on the electronic structure of lanthanides. It is worth noting that the order of OER mass activity of the catalyst is Ir₂Pr/G > Ir₂Nd/G > Ir₂Ce/G > Ir₂La/G > Ir/G. OER activity showed a volcanic relationship. A representative Ir₂Pr/G yielded a current density of 30.15 mA cm⁻² and a mass activity of 2.10 A mg⁻¹_{Ir} at 1.53 V

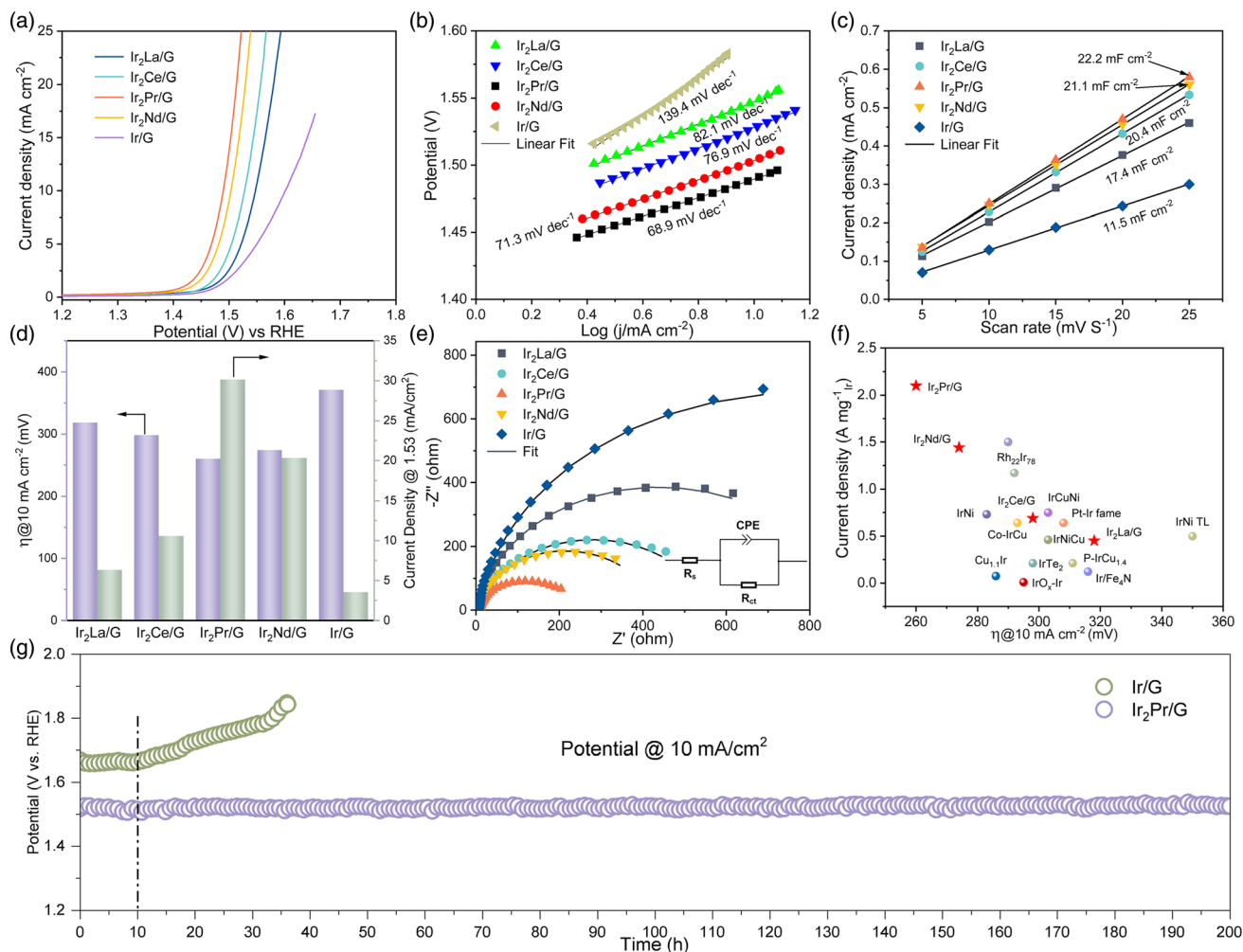


Figure 3. The electrochemical performance of Ir₂La/G, Ir₂Ce/G, Ir₂Pr/G, Ir₂Nd/G, and Ir/G in 0.5 M H₂SO₄ electrolyte. a) IR-corrected OER polarization curves. b) Tafel plots. c) C_{dl} curves by plotting current density versus scan rate. d) values of overpotential at a current density of 10 mA cm⁻² and current density at 1.53 V vs RHE. e) The Nyquist plots, inset is an equivalent circuit. f) Comparison of the overpotential at a current density of 10 mA cm⁻² and mass activity of the Ir-Ln nanoalloys with the representative reported Ir alloy OER catalysts. g) Chronopotentiometry curves for Ir₂Pr/G and Ir/G.

(vs RHE), respectively, improving the performance of Ir/G (a current density of 3.52 mA cm⁻² and a mass activity of 0.22 A mg⁻¹_{Ir}) by a factor of 8.6 and 9.5, which verifies the significant enhancement of electrocatalytic activity (Figure 3d). In addition, the EIS spectra of Ir₂La/G, Ir₂Ce/G, Ir₂Pr/G, Ir₂Nd/G, and Ir/G exhibit semicircular curves, which are in good agreement with the equivalent circuits (Figure 3e). The semicircle radius of the Ir alloy catalyst is smaller than that of Ir/G, which indicates that the alloying of Ir with Ln effectively accelerates the electron transfer in OER electrolysis. There was almost no difference in solution resistance (*R_s*) of all samples, among which Ir₂Pr/G had the smallest charge transfer resistance (*R_{ct}*) of 225.3 Ω, (Ir/G was 1548.0 Ω, Ir₂La/G was 870.2 Ω, Ir₂Ce/G was 550.8 Ω, and Ir₂Nd/G was 441.6 Ω), indicating the excellent charge transfer rate and electronic conductivity. The OER activities of Ir₂La/G, Ir₂Ce/G, Ir₂Pr/G, and Ir₂Nd/G in this work were compared with the mass activities and overpotentials of other previously reported and Ir-based catalysts, as shown in

Figure 3f.^[5,30–43] A comparison table with Ir and Ir alloy catalysts recently reported in the literature is shown in Table S4, Supporting Information. It is evident that among the Ir alloy catalysts, Ir₂Pr/G exhibits relatively high mass activity and low overpotential for OER. The stability of the alloy catalysts and Ir/G catalysts in OER was investigated. After 3000 consecutive cycles, the overpotentials of Ir₂La/G, Ir₂Ce/G, Ir₂Pr/G, and Ir₂Nd/G catalysts increased by only 6, 5, 4, and 4 mV, much lower than Ir/G (44 mV) (Figure S9, Supporting Information). After the stability test, the surface and the morphology of Ir₂Pr/G samples did not obviously change, supporting the robust electroactivity and durability (Figure S10, S11, Supporting Information). Meanwhile, alloying Ir with Ln achieves the dual improvement of catalytic activity and stability. In addition, Ir₂Pr/G was supported on carbon fibers to reduce the effect of bubbles on the catalyst surface to evaluate its lifetime. The Ir₂Pr/G catalyst was found to stably catalyze acidic OER at 10 mA cm⁻² for over 200 h (Figure 3g).

To reveal the electronic structures of Ir₂Ln alloys and their corresponding influences on the OER process, we have carried out systematic DFT calculations to investigate the electronic modulations and reaction trends. For the electronic distributions near the Fermi level (E_F), we have compared the Ir₂La and Ir₂Pr regarding the bonding and antibonding orbitals (Figure 4a). Notably, most of the surface electroactive regions are mostly dominated by the Ir sites, whereas the contributions from La sites are limited. The antibonding orbitals are slightly more evident on the surface, supporting the relatively lowered electroactivity. In comparison, the Pr sites on the surface of Ir₂Pr are actively involved in the bonding and antibonding orbitals, which are attributed to the appearance of 4f orbitals (Figure 4b). Moreover, the bonding orbitals are enriched on the surface of Ir₂Pr, leading to improved electron transfer and electroactivity toward the OER process. For both Ir₂Ln alloys, no evident lattice distortion is noted after the relaxation, which supports potentially high stability. Then, we further interpret the detailed electronic contributions of the electronic structures in the most electroactive Ir₂Pr (Figure 4c). It is noted that Ir-5d orbitals locate very close to the E_F , which play as the main active sites for the OER process. Meanwhile, the Pr-4f orbitals show strong

occupation crossing the E_F , which further alleviates the energy barriers of electron transfer from Ir sites. The Pr-5d orbitals dominate above the E_F , which overlaps with Pr-4f orbitals to support the fast electron transfer and protect Ir sites under the acidic media. Similar to Pr-4f orbitals, the Nd-4f orbitals also show strong occupation crossing the E_F , which alleviates the overall energy barriers for d-d electron transfer (Figure S12, Supporting Information). This leads to relatively good performances of Ir₂Nd toward OER. The Ce-4f orbitals also locate close to E_F , which also facilitates electron transfer with slightly larger energy barriers than Ir₂Pr and Ir₂Nd. In contrast, the Ir₂La shows no contributions from the 4f orbitals, where the significant energy barriers between Ir-5d and La-5d result in the lowest OER performances as experimental characterizations. Since the electrochemical performances of the OER are not linearly changed with the Ln elements, we have correlated the d-band center of Ir active sites with the overpotential (Figure 4d). Notably, the d-band center of Ir shows consistent changes with the overpotential, whereas the lower d-band center leads to the lower overpotential. This indicates that the slightly lowered d-band center of Ir sites potentially optimizes the binding strengths with the protons in the acidic media, which promotes

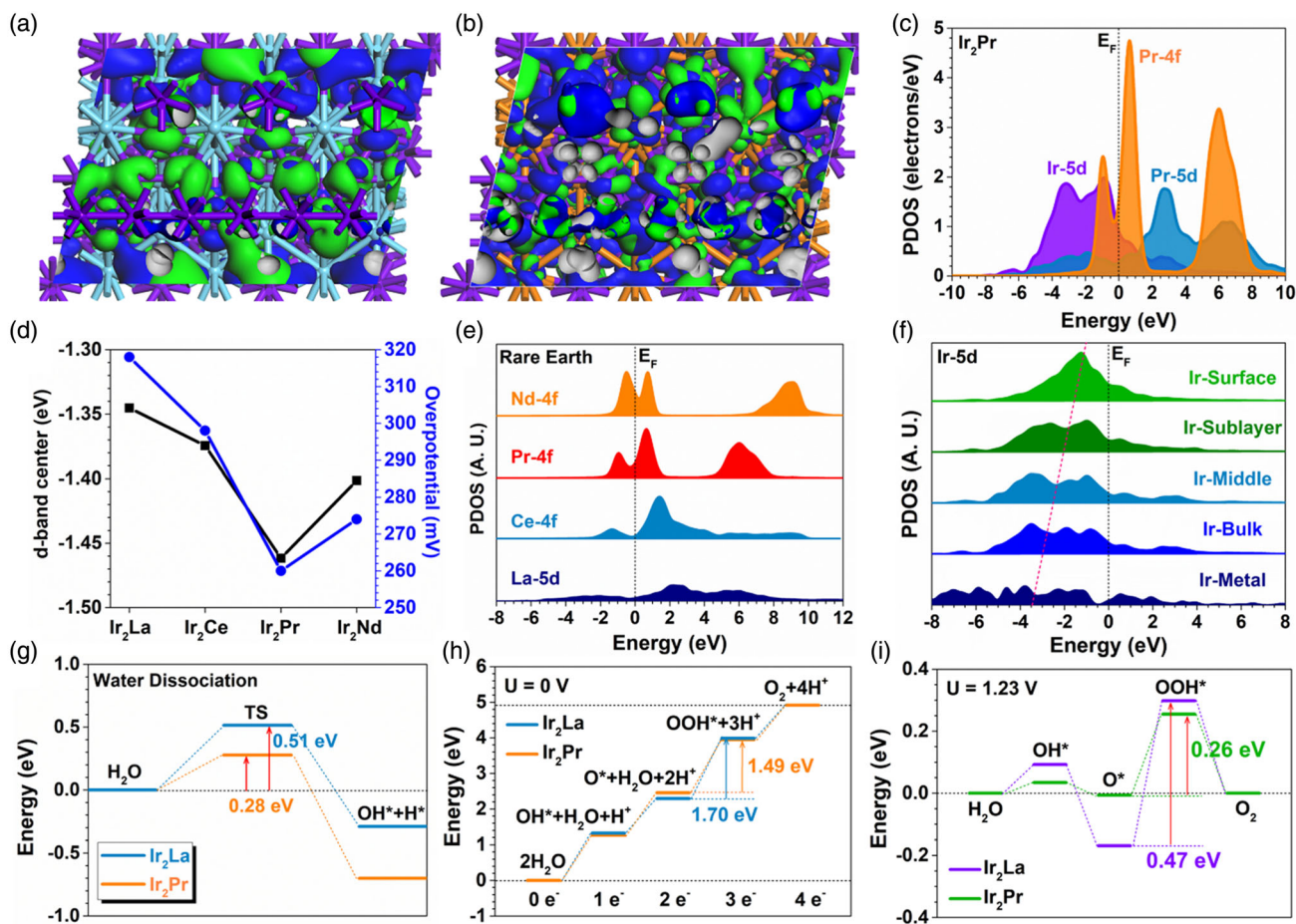


Figure 4. The 3D contour plot of electronic distribution near the Fermi level of a) Ir₂La and b) Ir₂Pr. Purple balls = Ir, Cyan balls = La, and Orange balls = Pr. Blue isosurface = bonding orbitals and Green isosurface = antibonding orbitals. c) The PDOS of Ir₂Pr. d) The correlation between the d-band center of surface Ir and overpotential. e) The PDOS of rare earth metals in the alloy. f) Site-dependent Ir-5d orbitals within Ir₂Pr. g) The water dissociation energy comparison of Ir₂La and Ir₂Pr. The reaction energy change of the acidic OER under h) $U = 0$ V and i) equilibrium potential of $U_{1.23} = V$.

the conversion of H₂O to facilitate the OER process. In the meantime, the overall d-band center still locates at a relatively high position to maintain the overall high electroactivity of the Ir₂Ln alloys. For RE metals, we notice a highly distinct trend in their electronic structures (Figure 4e). La-5*d* orbitals have shown a broad coverage with very low electron density near the E_F, which leads to the lowered electron transfer for the OER. For the 4*f* orbitals, we notice that Ce-4*f* orbitals display a much lower electron density than Pr-4*f* and Nd-4*f* orbitals. For Pr and Nd, their 4*f* orbitals are able to alleviate the electron depletion barrier from the alloy surface to the intermediates, which results in the highest electroactivity of the OER process. For different Ir sites within Ir₂Pr, the site-dependent PDOSs are demonstrated (Figure 4f). Compared to the Ir metal, the overall 5*d* orbitals of Ir sites within Ir₂Pr are much upshifted toward the E_F. From the bulk position to the surface, we notice a gradually upshifting trend of the 5*d* orbitals, which supports the increased electroactivity of the active sites, especially on the surface.

In the end, we have compared the reaction trend of the OER from the energetic perspective (Figure 4g). For the water dissociation, it is noted that Ir₂Pr shows a much smaller energy barrier of 0.28 eV than that of Ir₂La with a barrier of 0.51 eV, leading to a stronger reaction trend toward the OER. For the OER process without any applied potential (U = 0 V), the OER reactions exhibit a continuous uphill trend, where the conversion from O* to OOH* meets the largest energy barrier as the potential-determining step (Figure 4h). Ir₂Pr displays a smaller barrier than that of the Ir₂La for the acidic OER. With the applied equilibrium potential of 1.23 V, the overpotential of the OER has been estimated to be 0.26 and 0.47 V for Ir₂Pr and Ir₂La, respectively (Figure 4i). Notably, the initial step of forming OH* has shown a smaller barrier for Ir₂Pr, which is consistent with the water dissociation trends. The much increased overpotential of Ir₂La is attributed to the overbinding of O* due to the highest d-band center. Therefore, both electronic structure and energetic results have revealed the subtle modulations induced by RE elements and their influences on the acidic OER.

3. Conclusion

In conclusion, a rational reduction route was developed for the synthesis of Ir-RE nanoalloys. Ir-Ln (Ln = La, Ce, Pr, Nd) with uniform particle size was prepared on graphene as an efficient OER catalyst. In an acidic environment, the electronic structure of Ir is efficiently tailored by alloying with different RE elements. The relationship between lanthanide contraction and catalyst OER activity follows a “volcanic” relationship, and the catalytic activity and stability of the alloy catalysts are both improved. Ir₂Pr/G exhibits a mass activity of 2.10 A mg⁻¹_{Ir} and stability over 200 h, which is 9.5 times and 20 times that of the Ir/G catalyst. DFT calculations have revealed that the superior OER performance of Ir₂Pr is ascribed to the facilitation by the 4*f* orbitals in electron transfer and the lowest d-band center of active sites among Ir₂Ln alloys supply the optimized binding strength of the intermediates, which all guarantee the efficient OER process with lowered overpotential. In this work, the detailed study of the electron transfer mechanism of Ir-Ln nanoalloy catalysts is expected to lay a solid foundation for the novel design of RE

alloys in the future. This work will further expand the variety of RE alloy nanoalloy catalysts and paves the way for designing electrocatalysts with high catalytic activity and stability under harsh conditions.

4. Experimental Section

Chemicals: H₂IrCl₆·6H₂O (Ir ≥35%, Aladdin), Nafion solution (5 wt%, Alfa), CN₂H₂ (99%, Sigma-Aldrich), Ar gas (≥99.999%, H₂O ≤3 ppm, O₂ ≤2 ppm, Air Liquide), LaCl₃ (99.99%, Adamas), CeCl₃ (99.99%, Aladdin), PrCl₃ (99.99%, Aladdin), NdCl₃ (99.99%, Aladdin), graphene (SE1233, The Six Element, Inc.), H₂SO₄ (98%, Sinopharm), Na (99.9%, Aladdin), 2-propanol (99.9%, Aladdin), and Milli-Q water (≥18.2 MΩ cm). All the chemicals were used without further purification.

Catalyst Synthesis: 0.3 × g H₂IrCl₆·6H₂O, CN₂H₂, RE chloride (the mole ratio of Ir, Ln, and CN₂H₂ were 5:3:80), and 0.45 × g graphene were mixed in an agate mortar. The obtained mixture was then transferred into a boron nitride (BN) crucible for heat treatment. Then a Na ingot was placed in another BN crucible. These BN crucibles were placed in a big BN crucible (≈ 20 cm³ inner volume) so that the sodium vapor produced would only contact the powder mixture when heated. All the heat treatment of the sample was performed under inert gas (argon) using gloveboxes. The temperature was increased to 600 °C at the rate of 5 °C min⁻¹. It was kept at this temperature for 2 h, and it is cooled down to room temperature. After the heat treatment, the powder samples were washed with 2-propanol to remove residual sodium, and the remaining sodium in the BN crucible is recycled. The obtained product was transferred to the air and leached in 500 mL of 0.5 M H₂SO₄ at 40 °C for 1 h under continuous stirring. The product was then thoroughly washed with Milli-Q water and vacuum-dried at 70 °C for 5 h, yielding the final catalyst. The Ir/G was subjected to the same synthesis conditions but without the addition of LnCl₃ (the mole ratio of Ir and CN₂H₂ was 5: 80) for comparison.

Electrochemical Measurements: 2 mg synthesized catalysts were dispersed in a mixture of 490 μL ultrapure water, 490 μL isopropanol, and 20 μL Nafion solution, after sonication for 1 h. Electrochemical measurements were conducted on a CHI 660 E Electrochemical Workstation (Shanghai Chenhua Instrument Corporation, China) in a conventional three-electrode system. The graphite rod electrode is the counter electrode, a mercurous sulfate electrode is the reference electrode, and 0.5 M H₂SO₄ solution is the electrolyte (pH = 0.35). Every working electrode was activated by CV for 10 cycles with a sweep rate of 100 mV s⁻¹ before electrochemical measurements. All of the potentials were converted into the potential against reversible hydrogen electrode (RHE) based on the formulas, E(RHE) = E(Hg/Hg₂SO₄) + 0.656 + 0.0592 pH. Bubble high-purity Ar in the electrolyte for 30 min before measurement to exclude dissolved oxygen. The working electrode was a glassy carbon electrode (GCE, diameter: 5 mm, area: 0.196 cm²). 10 μL of the catalyst was dropped onto the GCE surface for further electrochemical tests. All the potentials reported in this work were converted to the RHE. OER performance was investigated by LSV at the scan rate of 5.0 mV s⁻¹. All the polarization curves were obtained with an ohmic potential drop (*iR*) correction arising from the solution resistance. Ohmic losses were corrected by subtracting the ohmic voltage drop from the measured potential, using the electrolyte resistance determined by the electrochemical impedance spectroscopy (EIS) at a high frequency where *iR*-corrected potentials were denoted as E - *iR*_s (*i* as the current and *R*_s as the electrolyte resistance). The Tafel slopes were derived from LSV curves at low overpotential fitted to the Tafel equation: η = a + b log*j*, where η is the overpotential, *b* is the Tafel slope, *j* is the current density, and *a* is the constant. The long-term durability of the catalyst was examined through chronopotentiometry at a constant current density of 10 mA cm⁻² to evaluate the durability of the samples supported on the carbon cloth. CV curves were collected at different scan rates (5, 10, 15, 20, and 25 mV s⁻¹) in a non-Faradaic potential window, which was measured from 1.21 to 1.31 V (vs RHE). The double-layer capacitance (C_{dl}) was obtained by plotting current densities (Δ*j*) at 1.26 V (vs RHE) against scan rates, and

the linear slope is twice the value of the calculated C_{dl} , where Δj stands for the different current density between anode and cathode. The CO oxidation experiments were carried out in 0.5 M H_2SO_4 solution for the CO stripping tests. Before the test, the solution was purged with argon for 30 min and then bubbled with CO gas (99.9%) for 15 min to achieve the maximum coverage of CO at the Ir active centers. The CO-stripping curves were recorded with a scan rate of 50 mV s^{-1} and the potential was set at 0.2–1.15 V (RHE). The ECSA was then calculated by dividing the integrated CO oxidation charge by 0.42 mC cm^{-2} . The ECSA was estimated from CO-stripping voltammetry using the following equation: $ECSA = S/V/0.42\text{ (mC cm}^{-2})/M_{Ir}$. Where S represents the CO stripping peak area, V represents the scan rates, and M_{Ir} represents the mass of Ir, respectively. The mass activity was calculated from the current density and mass loading of electrocatalysts at 1.53 V (vs RHE). The mass activity and specific activity were normalized by the mass of Ir metal (determined by the ICP tests). EIS measurements were measured at 1.45 V (vs RHE) in the frequency range from 100 kHz to 0.05 Hz with 5 mV amplitude in Ar saturated solution.

Physical Characterization: The powder XRD measurements were carried out on Rigaku Smart Lab 3 kW, an X-Ray diffraction diffractometer using monochromatized Cu $K\alpha$ radiation ($\lambda = 1.5418\text{ \AA}$). XPS were conducted using a Thermo Scientific ESCALAB 250Xi instrument equipped with an Al X-Ray excitation source. Transmission electron microscope (TEM) and high-angle annular dark-field scanning TEM images and energy-dispersive spectroscopy (EDS) were obtained using a field-emission TEM (JEM-2800, Japan). The contents of the electrocatalyst were analyzed by inductively coupled plasma mass spectrometry (Elan drc-e, USA). Data reduction, data analysis, and EXAFS fitting were performed and analyzed with the Athena and Artemis programs of the Demeter data analysis packages that utilize the FEFF6 program to fit the EXAFS data.^[44,45] The energy calibration of the sample was conducted through a standard Ir foil, which as a reference was simultaneously measured. A linear function was subtracted from the pre-edge region, then the edge jump was normalized using Athena software. The $\chi(k)$ data were isolated by subtracting a smooth, three-stage polynomial approximating the absorption background of an isolated atom. The k^3 -weighted $\chi(k)$ data were Fourier transformed after applying a Kaiser–Bessel window function ($\Delta k = 1.0$). For EXAFS modeling, the global amplitude EXAFS (CN, R, σ^2 , and ΔE_0) was obtained by nonlinear fitting, with least-squares refinement, of the EXAFS equation to the Fourier-transformed data in R-space, using Artemis software, EXAFS of the Ir foil is fitted and the obtained amplitude reduction factor S_0^2 value (0.829) was set in the EXAFS analysis to determine the coordination numbers (CNs) in the Ir-O/Pr/Ir scattering path in the sample.

Calculation Setup: In this work, we select the DFT within the CASTEP to investigate the electronic modulations induced by different RE elements in the Ir_2Ln alloys.^[46] The generalized gradient approximation and Perdew–Burke–Ernzerhof have been chosen to supply accurate descriptions of the exchange–correlation energy.^[47–49] Then, the cutoff energy has been set to 380 eV based on the ultrasoft pseudopotential scheme.^[50] The Broyden–Fletcher–Goldfarb–Shannon algorithm is applied with the coarse setting of the k-point mesh.^[51,52] The Ir_2Ln model has been built based on experimental characterizations with exposed (311) surfaces for the OER process. The following convergence criteria have been applied to guarantee the geometry optimizations including the Hellmann–Feynman forces should not exceed 0.001 eV \AA^{-1} ; the total energy and the ionic displacement should be smaller than $5 \times 10^{-5}\text{ eV atom}^{-1}$ and 0.005 \AA , respectively.

Supporting Information

Supporting Information is available from the Wiley Online Library or from the author.

Acknowledgements

The authors gratefully acknowledge the financial support from the National Key R&D Program of China (2021YFA1501101, 2017YFA0208000), the National Natural Science Foundation of China (21971117), the Functional

Research Funds for the Central Universities, Nankai University (63186005), the National Natural Science Foundation of China/Research Grant Council Joint Research Scheme (N_PolyU502/21), the Tianjin Key Lab for Rare Earth Materials and Applications (ZB19500202), the funding for Projects of Strategic Importance of The Hong Kong Polytechnic University (Project Code: 1-ZE2V), Departmental General Research Fund (Project Code: ZVUL) of The Hong Kong Polytechnic University, Shenzhen Fundamental Research Scheme-General Program (JCYJ20220531090807017), the Open Funds (No. RERU2019001) of the State Key Laboratory of Rare Earth Resource Utilization, the 111 Project (No. B18030) from China, the Outstanding Youth Project of Tianjin Natural Science Foundation (20JCQJC00130), and the Key Project of Tianjin Natural Science Foundation (20JCZDJC00650). The authors also thank the Haihe Laboratory of Sustainable Chemical Transformations for financial support. This work was also supported by the Ph.D. Candidate Research Innovation Fund of NKU School of Materials Science and Engineering. B.H. also thanks the support from the Research Centre for Carbon-Strategic Catalysis (RC-CSC), Research Institute for Smart Energy (RISE), and Research Institute for Intelligent Wearable Systems (RI-IWEAR) of the Hong Kong Polytechnic University.

Data Availability Statement

The authors declare no conflict of interest.

Conflict of Interest

The data that support the findings of this study are available from the corresponding author upon reasonable request.

Keywords

acidic oxygen evolution, electronic structure tailoring, high mass activity, ir-based electrocatalysts, rare earth alloys

Received: February 8, 2023

Revised: March 17, 2023

Published online: April 3, 2023

- [1] D. Wakerley, S. Lamaison, J. Wicks, A. Clemens, J. Feaster, D. Corral, S. A. Jaffer, A. Sarkar, M. Fontecave, E. B. Duoss, S. Baker, E. H. Sargent, T. F. Jaramillo, C. Hahn, *Nat. Energy* **2022**, *7*, 130.
- [2] A. Li, S. Kong, C. Guo, H. Ooka, K. Adachi, D. Hashizume, Q. Jiang, H. Han, J. Xiao, R. Nakamura, *Nat. Catal.* **2022**, *5*, 109.
- [3] H. Nguyen, C. Klose, L. Metzler, S. Vierrath, M. Breitwieser, *Adv. Energy Mater.* **2022**, *12*, 2103559.
- [4] L. Zhao, J. Zhu, Y. Zheng, M. Xiao, R. Gao, Z. Zhang, G. Wen, H. Dou, Y.-P. Deng, A. Yu, Z. Wang, Z. Chen, *Adv. Energy Mater.* **2022**, *12*, 2102665.
- [5] Q. Zhuang, N. Ma, Z. Yin, X. Yang, Z. Yin, J. Gao, Y. Xu, Z. Gao, H. Wang, J. Kang, D. Xiao, J. Li, X. Li, D. Ma, *Adv. Energy Sustain. Res.* **2021**, *2*, 2100030.
- [6] S. Pedram, M. Batool, K. Yapp, L. Bonville, J. Jankovic, *Adv. Energy Sustain. Res.* **2021**, *2*, 2000092.
- [7] X. Liu, Y. Han, Y. Guo, X. Zhao, D. Pan, K. Li, Z. Wen, *Adv. Energy Sustain. Res.* **2022**, *3*, 2200005.
- [8] Q. Zhuang, N. Ma, Z. Yin, X. Yang, Z. Yin, J. Gao, Y. Xu, Z. Gao, H. Wang, J. Kang, D. Xiao, J. Li, X. Li, D. Ma, *Adv. Energy Sustain. Res.* **2021**, *2*, 2100030.
- [9] J. Zhu, M. Xie, Z. Chen, Z. Lyu, M. Chi, W. Jin, Y. Xia, *Adv. Energy Mater.* **2020**, *10*, 1904114.

- [10] J. Wang, L. Han, B. Huang, Q. Shao, H. L. Xin, X. Huang, *Nat. Commun.* **2019**, *10*, 5692.
- [11] S. Hao, H. Sheng, M. Liu, J. Huang, G. Zheng, F. Zhang, X. Liu, Z. Su, J. Hu, Y. Qian, L. Zhou, Y. He, B. Song, L. Lei, X. Zhang, S. Jin, *Nat. Nanotechnol.* **2021**, *16*, 1371.
- [12] J. Kibsgaard, I. Chorkendorff, *Nat. Energy* **2019**, *4*, 430.
- [13] T. Shen, S. Wang, T. Zhao, Y. Hu, D. Wang, *Adv. Energy Mater.* **2022**, *12*, 2201823.
- [14] J. Song, C. Wei, Z. F. Huang, C. Liu, L. Zeng, X. Wang, Z. J. Xu, *Chem. Soc. Rev.* **2020**, *49*, 2196.
- [15] M. Escudero-Escribano, P. Malacrida, M. H. Hansen, U. G. Vej-Hansen, A. Velazquez-Palenzuela, V. Tripkovic, J. Schiøtz, J. Rossmeisl, I. E. L. Stephens, I. Chorkendorff, *Science* **2016**, *352*, 73.
- [16] S. Zhang, S. E. Saji, Z. Yin, H. Zhang, Y. Du, C. H. Yan, *Adv. Mater.* **2021**, *33*, e2005988
- [17] S. Zhang, Z. Zeng, Q. Li, B. Huang, X. Zhang, Y. Du, C. H. Yan, *Energy Environ. Sci.* **2021**, *14*, 5911.
- [18] Y. T. Gong, J. Z. Wu, M. Kitano, J. J. Wang, T. N. Ye, J. Li, Y. Kobayashi, K. Kishida, H. Abe, Y. Niwa, H. S. Yang, T. Tada, H. Hosono, *Nat. Catal.* **2018**, *1*, 178.
- [19] Y. Hu, J. O. Jensen, L. N. Cleemann, B. A. Brandes, Q. Li, *J. Am. Chem. Soc.* **2020**, *142*, 953.
- [20] Y. Yan, J. S. Du, K. D. Gilroy, D. Yang, Y. Xia, H. Zhang, *Adv. Mater.* **2017**, *29*, 1605997.
- [21] J. Li, S. Sun, *Acc. Chem. Res.* **2019**, *52*, 2015.
- [22] A. Morozkin, Y. D. Seropegin, A. Gribanov, J. Barakatova, *Compounds* **1997**, *256*, 175.
- [23] Z. Blazina, R. C. Mohanty, A. Raman, *Int. J. Mater. Res.* **1989**, *80*, 192.
- [24] F. Greidanus, L. De Jongh, W. Huiskamp, A. Furrer, K. Buschow, in *Crystalline Electric Field Effects in f-Electron Magnetism*, Springer, New York, NY **1982**, 13.
- [25] S. J. Freakley, J. R. Esquius, D. J. Morgan, *Surf. Interface Anal.* **2017**, *49*, 794.
- [26] A. Fujimori, J. Osterwalder, *J. Phys. C: Solid State Phys.* **1984**, *17*, 2869.
- [27] C. J. Powell, *J. Electron Spectrosc.* **2012**, *185*, 1.
- [28] E. Bourbos, A. Karantonis, L. Sygellou, I. Paspaliaris, D. Panias, *Metals* **2018**, *8*, 803.
- [29] H. Ota, M. Matsumiya, N. Sasaya, K. Nishihata, K. Tsunashima, *Electrochim. Acta* **2016**, *222*, 20.
- [30] H. Guo, Z. Fang, H. Li, D. Fernandez, G. Henkelman, S. M. Humphrey, G. Yu, *ACS Nano* **2019**, *13*, 13225.
- [31] Y. Pi, Y. Xu, L. Li, T. Sun, B. Huang, L. Bu, Y. Ma, Z. Hu, C. W. Pao, X. Huang, *Adv. Funct. Mater.* **2020**, *30*, 2004375.
- [32] S. Choi, J. Park, M. K. Kabiraz, Y. Hong, T. Kwon, T. Kim, A. Oh, H. Baik, M. Lee, , *Adv. Funct. Mater.* **2020**, *30*, 2070253.
- [33] Y. Wang, L. Zhang, K. Yin, J. Zhang, H. Gao, N. Liu, Z. Peng, Z. Zhang, *ACS Appl. Mater. Inter.* **2019**, *11*, 39728.
- [34] B. M. Tackett, W. Sheng, S. Kattel, S. Yao, B. Yan, K. A. Kuttiyiel, Q. Wu, , *ACS Catal.* **2018**, *8*, 2615.
- [35] Q. Shi, C. Zhu, H. Zhong, D. Su, N. Li, M. H. Engelhard, H. Xia, Q. Zhang, S. Feng, , *ACS Energy Lett.* **2018**, *3*, 2038.
- [36] Y. Pi, J. Guo, Q. Shao, M. Huang, *Chem. Mater.* **2018**, *30*, 8571.
- [37] Y. Pi, Q. Shao, P. Wang, J. Guo, X. Huang, *Adv. Funct. Mater.* **2017**, *27*, 1700886.
- [38] J. Park, Y. J. Sa, H. Baik, T. Kwon, S. H. Joo, K. Lee, *ACS Nano* **2017**, *11*, 5500.
- [39] T. Kwon, H. Hwang, Y. J. Sa, J. Park, H. Baik, S. H. Joo, K. Lee, *Adv. Funct. Mater.* **2017**, *27*, 1604688.
- [40] Y. Pi, N. Zhang, S. Guo, J. Guo, X. Huang, *Nano Lett.* **2016**, *16*, 4424.
- [41] J. Lim, S. Yang, C. Kim, C. W. Roh, Y. Kwon, Y. T. Kim, H. Lee, *Chem. Commun.* **2016**, *52*, 5641.
- [42] P. Lettenmeier, L. Wang, U. G. Schindler, P. Gazdzicki, N. A. Cañas, M. Handl, R. Hiesgen, S. S. Hosseiny, A. S. Gago, K. A. Friedrich, *Angew. Chem. Int. Ed.* **2016**, *128*, 752.
- [43] C. Wang, Y. Sui, G. Xiao, X. Yang, Y. Wei, G. Zou, B. A. Zou, **2015**, *3*, 19669.
- [44] B. Ravel, M. Newville, *J. Synchrotron Radiat.* **2005**, *12*, 537.
- [45] S. I. Zabinsky, J. J. Rehr, A. Ankudinov, R. C. Albers, M. J. Eller, *Phys. Rev. B* **1995**, *52*, 2995.
- [46] S. J. Clark, M. D. Segall, C. J. Pickard, P. J. Hasnip, M. J. Probert, K. Refson, M. C. Payne, *Z. Kristallogr. Krist.* **2005**, *220*, 567.
- [47] J. P. Perdew, K. Burke, M. Ernzerhof, *Phys. Rev. Lett.* **1996**, *77*, 3865.
- [48] P. J. Hasnip, C. J. Pickard, *Comput. Phys. Commun.* **2006**, *174*, 24.
- [49] J. P. Perdew, J. A. Chevary, S. H. Vosko, K. A. Jackson, M. R. Pederson, D. J. Singh, C. Fiolhais, *Phys. Rev. B* **1992**, *46*, 6671.
- [50] D. Vanderbilt, *Phys. Rev. B* **1990**, *41*, 7892.
- [51] J. D. Head, M. C. Zerner, *Chem. Phys. Lett.* **1985**, *122*, 264.
- [52] M. I. J. Probert, M. C. Payne, *Phys. Rev. B* **2003**, *67*, 75204.